

REPORTS

(20), and the molecular outflow speed is ~ 2 km s⁻¹, implying a scale length for production of atomic carbon from CO that is greater than the width of the observed plasma tail. Clearly a source of atomic carbon independent of CO is required.

Although UVCS cannot see the dust tail, dust is the most likely source of atomic carbon. One model of comet composition describes cometary nuclei as aggregates of interstellar dust grains swept up from the outer regions of the presolar nebula (21). These grains are believed to acquire organic refractory coatings during their prolonged exposure to the cold interstellar medium. These coatings begin to evaporate at about 500 K. A typical submicron dust grain has a predicted temperature of ≈ 1300 K at 0.2 AU (22). Indeed, the dust tail of Kudo-Fujikawa as imaged by LASCO was faint, which might reflect depletion of the tail as a result of evaporation of the dust grains. Carbon evaporated from the dust will be photoionized relatively quickly to C⁺ and C²⁺.

Finally, there is a potentially interesting parallel between our observations and a phenomenon observed in the extensively studied β Pictoris (Pic) system. The often-imaged disk surrounding β Pic is believed to consist of debris from the collisional destruction of planets and planetesimals. The presence of variable absorption lines of Al III, C IV, and other ionized metallic species has been explained by a model in which kilometer-sized cometary bodies evaporate as they fall toward the star (23). We note that the optical thickness of the C III 97.7-nm line in Kudo-Fujikawa is $\tau \sim 0.6$, sufficient to make such a line readily detectable in absorption against the strong, broad C III emission line of β Pic. If a stellar wind is present, the plasma tail will stream away from the star, giving the absorption feature a distinctive, blue-shifted profile. Indeed, a recent study of β Pic detected the C III multiplet at 117.6 nm and inferred the presence of a weak stellar wind (24). A weak, narrow absorption feature with a blueshift of ~ 200 km s⁻¹ was marginally detected in the line profile of C III 97.7 nm. Further work on this subject should strengthen the connection between solar system comets and their extrasolar counterparts, both sharing an origin in interstellar dust.

References and Notes

1. J. C. Brandt, M. Snow, *Icarus* **148**, 52 (2000).
2. S. Nakano, *Int. Astron. Union Circ.* **8032** (2002).
3. J. Watanabe, *Int. Astron. Union Circ.* **8033** (2002).
4. J. L. Kohl et al., *Sol. Phys.* **162**, 313 (1995).
5. J. C. Raymond et al., *Astrophys. J.* **564**, 1054 (2002).
6. M. R. Combi, W. H. Smyth, *Astrophys. J.* **327**, 1026 (1988).
7. We used solar spectra from the Thermosphere Ionosphere Mesosphere Energetics and Dynamics/Solar EUV Experiment mission (25) to obtain the ionizing flux at the time of our observations. We thus obtained a photoionization rate coefficient of

- 3.52×10^{-6} s⁻¹ for neutral H. The charge-transfer rate coefficient for H is taken to be 7.1×10^{-6} s⁻¹, and the electron-impact rate coefficient is 1.5×10^{-6} s⁻¹.
8. The g factor is the number of Ly α photons scattered per second by an H atom in the coma. We used the solar spectrum of Curdt et al. (26), scaled by a factor of 1.6 to account for solar maximum conditions, to compute the g factors for Ly α and the other spectral lines used in our analysis.
9. We treat the slow component of the H distribution as a narrow ($\Delta v_1 = 10$ km s⁻¹), more optically thick profile superimposed upon the broad ($\Delta v_2 = 40$ km s⁻¹) profile of the fast component.
10. M. Bout, P. Lamy, A. Llebaria, *Bull. Am. Astron. Soc.* **35**, 988 (2003).
11. The photoionization cross sections for C and O atoms and ions were computed with the use of the method of Verner et al. (27). With the use of the TIMED/SEE spectrum, we derived rate coefficients, q , for carbon ions of $q(\text{C I}) = 2.93 \times 10^{-5}$ s⁻¹, $q(\text{C II}) = 2.79 \times 10^{-6}$ s⁻¹, and $q(\text{C III}) = 4.12 \times 10^{-7}$ s⁻¹.
12. H. Alfvén, *Tellus* **9**, 92 (1957).
13. T. I. Gombosi et al., *J. Geophys. Res.* **101**, 15223 (1996).
14. Y. Yi et al., *J. Geophys. Res.* **101**, 27585 (1996).
15. Information is available online at www.sp.ph.ic.ac.uk/~jonesg/comets_sun.
16. Information is available online at <http://quake.stanford.edu/~wso/SYNOP/1999.250r.gif>.
17. N. R. Sheeley Jr. et al., *J. Geophys. Res.* **104**, 24739 (1999).

18. M. A. DiSanti, et al., *Icarus* **153**, 361 (2001).
19. P. D. Feldman, H. A. Weaver, E. B. Burgh, *Astrophys. J.* **576**, L91 (2002).
20. W. F. Huebner, J. J. Keady, S. P. Lyon, *Adv. Space Sci.* **195** 1 (1992).
21. J. M. Greenberg, A. Li, *Space Sci. Rev.* **90**, 149 (1999).
22. P. L. Lamy, J.-M. Perrin, *Icarus* **76**, 100 (1988).
23. A. Vidal-Madjar, A. Lecavelier des Etangs, R. Ferlet, *Planet. Space Sci.* **46**, 629 (1998).
24. J.-C. Bouret et al., *Astron. Astrophys.* **390**, 1049 (2002).
25. T. N. Woods et al., *SPIE Conf. Proc.* **3442**, 180 (1998).
26. W. Curdt et al., *Astron. Astrophys.* **375**, 591 (2001).
27. D. A. Verner et al., *Astrophys. J.* **465**, 487 (1996).
28. This work was supported primarily by NASA grant NAG5-12814. Additional support was provided by NASA grants NAG5-12865 and NAG5-11420 (UVCS/SOHO), NAG5-9059 (Planetary Atmospheres), and NAG5-12668 (Laboratory Astrophysics). This research was performed while G.H.J. held a National Research Council Research Associateship Award at NASA Jet Propulsion Laboratory. G.H.J. is a SOHO Guest Investigator. We thank P. Lamy for providing data from SOHO/LASCO.

Supporting Online Material

www.sciencemag.org/cgi/content/full/302/5652/1949/DC1
Fig. S1

2 October 2003; accepted 13 November 2003

Direct Observations of North Pacific Ventilation: Brine Rejection in the Okhotsk Sea

Andrey Y. Shcherbina, Lynne D. Talley,* Daniel L. Rudnick

Brine rejection that accompanies ice formation in coastal polynyas is responsible for ventilating several globally important water masses in the Arctic and Antarctic. However, most previous studies of this process have been indirect, based on heat budget analyses or on warm-season water column inventories. Here, we present direct measurements of brine rejection and formation of North Pacific Intermediate Water in the Okhotsk Sea from moored winter observations. A steady, nearly linear salinity increase unambiguously caused by local ice formation was observed for more than a month.

The global thermohaline circulation is primed by dense water formation in high latitudes, which leads to the gradual renewal of the deep ocean. The densest bottom water is formed in the North Atlantic and Southern Oceans. Ventilation of the intermediate layer of the ocean, however, is just as important for the global overturning circulation as is deep water formation in terms of mass, heat, and freshwater transport (1). North Pacific Intermediate Water (NPIW), the densest water formed in the North Pacific, is therefore a key water mass in the general circulation. NPIW is bounded at its

top by a minimum in the vertical salinity distribution throughout the North Pacific subtropical gyre at 26.7 to 26.8 σ_θ (2, 3) and extends down to 27.6 σ_θ , on the basis of tracers indicating renewal (4). Because NPIW isopycnals do not outcrop in the open North Pacific, ventilation by deep convection, such as in the North Atlantic, can be ruled out. Instead, this overturn is driven by wintertime brine rejection in the Sea of Okhotsk (Fig. 1), the southernmost sea with considerable seasonal ice cover in the Northern Hemisphere (4–6).

Rejection of salty brine, which invariably accompanies the freezing of seawater, creates some of the densest water masses in the world ocean. As the new sea ice, which is typically 70 to 90% fresher than the seawater (7), forms, the expelled brine

Scripps Institution of Oceanography, University of California, San Diego, USA.

*To whom correspondence should be addressed. E-mail: ltalley@usc.edu

causes substantial density increase and stability loss in the underlying water column. Similarly to thermal convection, brine rejection can lead to rapid water-mass transformation, bringing surface waters to deeper density levels. On the basis of water properties observed primarily at the end of the ice-covered season, brine rejection has been hypothesized to be responsible for ventilation of deep and intermediate waters in the Arctic and Antarctic (8–10). Sparse winter hydrographic and mooring observations have found brine-rejection signatures in the Bering (11), Chukchi (12), Ross (13), and Japan (14) Seas, and off the Adélie Land coast of Antarctica (15). However, the continuous temporal evolution of a water mass solely due to brine rejection has not been reported.

Coastal polynyas (extensive areas of open water or thinner ice within a pack ice field) are the most active regions of brine production, because the amount of expelled brine is greatest during the initial stages of ice formation. Water inside the polynyas, which are commonly encountered along the coastal margins because of offshore winds, is in direct contact with cold air, which leads to severe heat loss and continuous ice production. Several persistent polynyas are observed along the northern and western shores of the Okhotsk Sea each winter (Fig. 1B). The high ice production, combined with the downstream location of the northwestern polynya with respect to the cyclonic circulation in the northern Okhotsk Sea, explains the summertime observations of the coldest ($<-1^{\circ}\text{C}$) and densest (26.8 to $27.2 \sigma_{\theta}$) water in that region (5, 6). This dense shelf water (DSW) is advected southward along the eastern coast of Sakhalin, where vertical mixing alters its structure

and extends its influence to higher densities (4). Even though DSW originates as high-salinity brine, its near-freezing temperature accounts for its being relatively fresh compared with the surrounding waters of the same density (4). Eventually DSW, severely modified by mixing but retaining its low-salinity signature, is exported into the Pacific, ventilating the NPIW in both subpolar and subtropical gyres.

The process of dense water formation in the Okhotsk Sea closely resembles that found in other polar marginal seas. In some aspects, however, such as vertical distribution of plankton species, the Okhotsk Sea is distinctive, with the closest analog being the subpolar conditions all over the globe during the Last Glacial Maximum (16). During that time the northern Okhotsk Sea likely retained its importance as the site of NPIW formation (17), which, however, was more vigorous than at present (17). Severe wintertime conditions, shallow shelves, and easy summertime access make the Okhotsk Sea convenient for studying brine rejection in coastal polynyas.

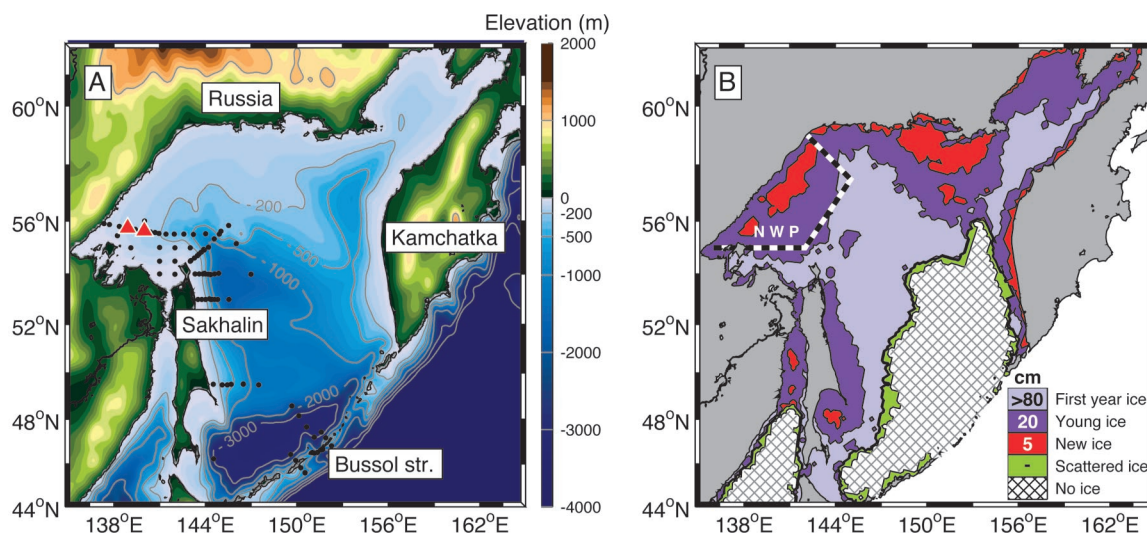
The northwestern shelf was the primary target of the present study. DSW is present for most of the year as a bottom temperature minimum on the shelf north of Sakhalin, extending into the East Sakhalin current (5, 6, 18). Even in autumn (Fig. 2A), the bottom potential temperature was within 0.1°C of freezing. The layer of “old” DSW formed during the previous winter was ~ 30 m thick along the bottom between the 100- and 160-m isobaths, with a maximum density of $26.93 \sigma_{\theta}$ observed at 150 m (Fig. 2B). To observe wintertime DSW evolution, in September 1999 a bottom mooring array was deployed on the northwestern shelf (Fig. 1). Four moorings were

deployed within the DSW layer, and two were successfully recovered in June 2000. Vertical profiles of current speed, as well as temperature, salinity, and pressure at the bottom were measured (19).

According to our observations, the starting point of DSW formation was not the DSW from previous winters, as was assumed earlier (20), but fresher, lighter tidally mixed near-shore water (NSW). This water appears on the shelf in a narrow band along the coast (less than 100 m deep) in spring and summer, chiefly as a result of sea ice melt. A shelf front (temperature and potential density change of 10°C and 2 kg m^{-3} over 100 km distance, respectively) (Fig. 2B) marked the outer boundary of NSW in September. In late autumn, the front moved offshore as the surface cooling weakened the shelf stratification. An abrupt salinity drop and temperature increase marked the passage of the front through the site of the western mooring in mid-November (Fig. 3). This offshore transition of the front, also seen on satellite sea surface temperature imagery (not shown), displaced the “old” DSW from the formation region. Consequently, the starting point for new DSW formation was almost 0.4 practical salinity units (PSU) fresher than had been previously inferred from warm-season observations (20). The lower initial salinity affects the estimates of DSW production based on surface heat flux models (6, 20), as it decreases the maximum density produced by a given heat loss.

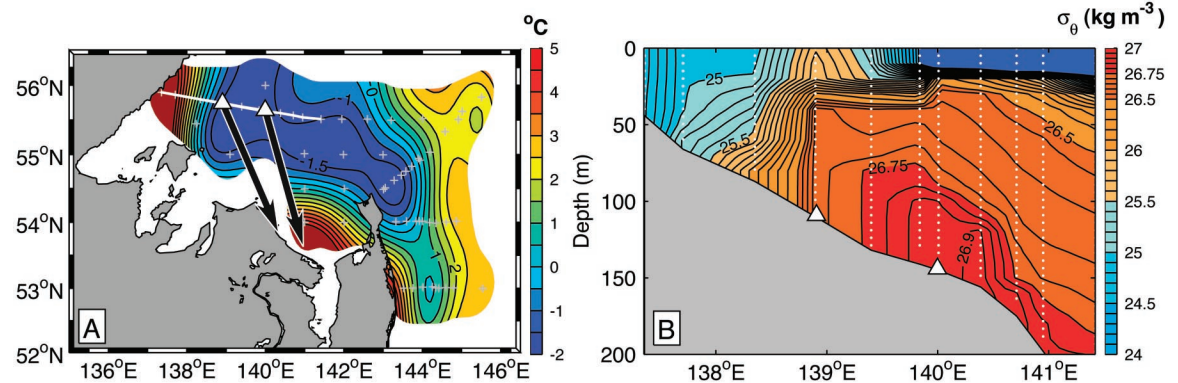
DSW formation by brine rejection is unmistakable in the salinity, potential temperature, and potential density time series (Fig. 3). A salinity increase associated with brine rejection started at the western mooring on 20 January, soon after ice cover at

Fig. 1. The Okhotsk Sea. The topographic map (A) shows station positions of the September 1999 survey (dots) and bottom mooring positions (red triangles). (B) Ice distribution on the basis of National Snow and Ice Data Center special sensor microwave imager (SSM/I) brightness temperatures (27) and the Cavalieri “thin ice” algorithm (28). Numbers on the legend indicate typical thicknesses of the ice types (in cm), according to (29). Cross-hatching defines ice-free regions. The dashed line marks the assumed boundaries of the northwestern polynya (NWP) shelf region.



REPORTS

Fig. 2. Dense water on the northwestern shelf, 6 to 20 September 1999. **(A)** Bottom potential temperature. Arrows show direction of the mean flow at the bottom moorings from September to June (average speed is 6.3 cm s^{-1} for both). **(B)** Potential density along the 56°N section, shown by white line in **(A)**. Positions of stations (vertical dotted lines) and the bottom moorings (triangles) are shown.



the site was established. A near-linear salinity increase continued through 23 February, reaching a maximum salinity of 33.45 PSU, for a total salinity increase of 0.83 PSU in 35 days. This corresponds to a 0.68 kg m^{-3} potential density increase, reaching a maximum potential density of 26.92 kg m^{-3} . The observed salinity and density changes could not be explained by a shift in water masses, because no water of sufficient salinity was present on the shelf in autumn. Daily ice growth of 13 cm (4.6 m total) would produce the observed salinity increase, which is consistent with the observed local heat fluxes (Fig. 4), given the uncertainties of these estimates. Potential temperature stayed at the freezing point throughout this period, further supporting the leading role of brine rejection. The termination of the density increase was markedly abrupt and, according to satellite observations, was not associated with the polynya closure. A subsequent short-term salinity burst on 15 to 17 March produced an absolute maximum salinity of 33.49 PSU ($26.95 \sigma_\theta$). A steady salinity decrease through the remainder of the western mooring record suggests gradual flushing of DSW with fresher water from the northern shelves.

The offshore boundary of the newly formed DSW appeared to be sharp and located between the two moorings. No direct signature of dense water formation was found at the eastern mooring, even though the moorings were less than 70 km apart. Instead, a slow, steady salinity increase was observed from 16 January to the end of the record in June, probably due to gradual export of dense water from the polynya. As the brine rejection progressed, the density front between the stations was first eliminated (on 1 February) and then reestablished at virtually the same location but with the opposite density gradient. This result suggests that DSW completely replaced NSW by the end of the ice formation season.

Surface heat loss leading to ice forma-

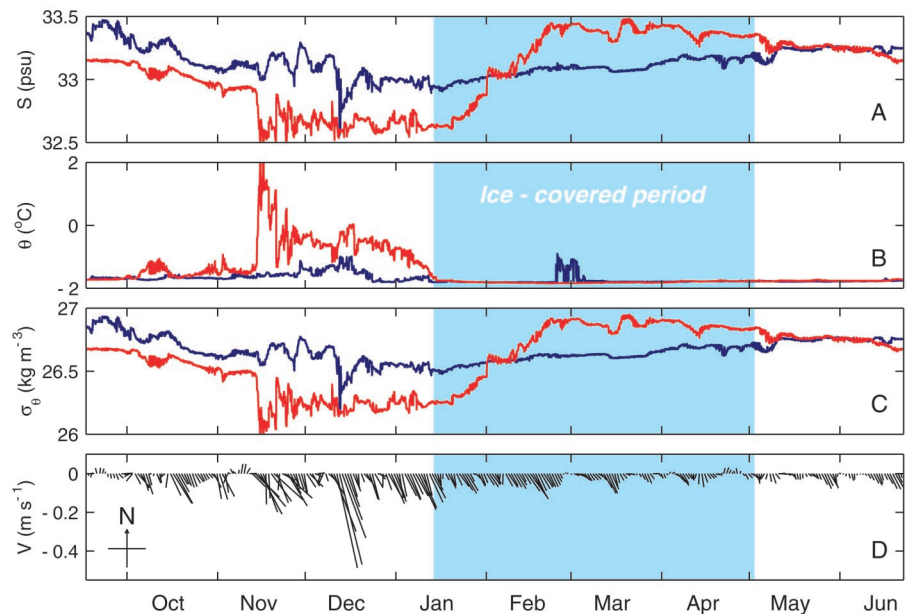


Fig. 3. Bottom water properties at the moorings. **(A)** Salinity, **(B)** potential temperature, and **(C)** potential density on the western (red line) and eastern (blue line) bottom moorings. **(D)** Mean horizontal velocity vector at the western bottom mooring low-passed with a 4-day Blackman filter. Blue shading indicates persistent ice cover over the western mooring, as detected by the mooring's Acoustic Doppler Current Profiler.

tion in the polynya is the driving mechanism of brine rejection. The observed ice cover over the northern and northwestern shelves stayed close to 100% from mid-January to early April, but the "new" and "young" ice fractions with a typical thickness of less than 30 cm dominated inside the polynya regions (Fig. 4A), allowing large heat loss. The thin ice was gradually replaced by thicker first-year ice as the winter progressed, and the polynyas were virtually closed by mid-March.

Estimation of heat flux on the basis of remote sensing of ice concentrations and atmospheric data reanalysis (20) remains the only means of studying dense water formation in most polynyas. Our in situ observations show the limitations of this approach in predicting both temporal and

spatial extent of DSW formation. Peak brine rejection generally coincided with maximum heat loss in the northwestern polynya, but the observed period of DSW densification from mid-January to late February was shorter than can be predicted from surface flux data alone (Fig. 4B). The onset of bottom water modification was apparently delayed by the time necessary to eliminate seasonal stratification (about a week after the start of freezing). The abrupt termination of DSW density increase almost three weeks before the polynya closure suggests the enhancement of lateral dispersion of the density anomaly. According to numerical models, baroclinic instability at the front bounding the formation region can similarly limit the density increase (21).

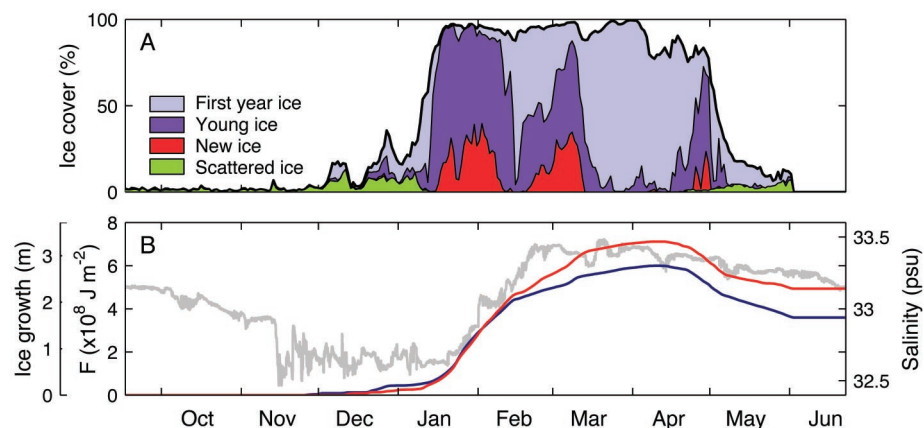


Fig. 4. Evolution of northwestern polynya. **(A)** Fractional ice cover over the northwestern shelf (within 50- to 200-m depth interval and the boundaries shown in Fig. 1B). **(B)** Cumulative heat loss through the ice above the western (red line) and eastern (blue line) mooring site. The leftmost scale shows the ice growth equivalent to this heat loss. Salinity at the western mooring (gray line) is shown for reference. The estimates of heat fluxes and ice classification are based on European Centre for Medium-Range Weather Forecasts reanalysis meteorology and National Snow and Ice Data Center ice data, respectively.

The lateral extent of DSW penetration to the bottom did not coincide with the polynya boundaries defined from ice concentration and heat-loss maps. The heat loss over the two moorings differed by only 20% (Fig. 4B), suggesting that both instruments were located within the polynya, yet the salinity increase observed at the western mooring from January to March was more than five times as large as that at the eastern mooring. This result suggests that the boundaries of newly formed DSW were strongly affected by the flow dynamics in addition to the surface forcing.

General cyclonic circulation in the Okhotsk Sea is the primary mechanism of exporting DSW from the formation region. Predominantly southward terrain-following flow with a mean speed of $\sim 6.3 \text{ cm s}^{-1}$ (Fig. 2A) was observed at both moorings. Low-passed horizontal velocity (Fig. 3D) shows a general increase of southward flow between October and January, with weaker flow during the ice-covered period, consistent with changes in the large-scale wind forcing (22). Southward dense water transport can be estimated by using the observed velocities and assuming that the outer margin of dense water was located between the moorings. If the new dense water extends all the way to shore and to the surface, its cross section can be estimated as $(12.5 \pm 4.5) \times 10^6 \text{ m}^2$, with the uncertainty being half the cross-section area between the moorings. Using a mean advection velocity of 6 cm s^{-1} (January and February), we calculated the winter dense water transport as roughly $0.75 \pm 0.28 \text{ Sv}$ ($1 \text{ Sv} = 10^6 \text{ m}^3 \text{ s}^{-1}$). The transport drops to $\sim 0.34 \pm 0.12 \text{ Sv}$ in spring (March and April) as a result of decreased velocity. A more reliable estimate of the dense water

cross section is possible at the times of the pre- and postcruise sections. Defining DSW as water denser than $26.7 \sigma_\theta$ and colder than -1°C , the cross section was $6.9 \times 10^6 \text{ m}^2$ in September and $7.7 \times 10^6 \text{ m}^2$ in June. Mean velocities are taken from the first and last week of the record of the eastern mooring, because it was located in the core of the dense water during these periods. The resulting estimate is 0.33 Sv in June and 0.02 Sv in September.

Our estimates of DSW production support previous indirect estimates. Variation in annual DSW formation rates between 0.2 and 0.5 Sv , depending on the winter conditions for a given year, has been inferred from remotely sensed ice production rates and nonwinter hydrographic surveys (6, 20). Seasonal change from $1.4 \pm 1.2 \text{ Sv}$ during February through May to $0.2 \pm 0.1 \text{ Sv}$ in summer has also been suggested by historical hydrographic data analyzed for the Kuril Basin (18).

Theoretical and observational studies in the North Atlantic and Arctic Oceans (23, 24) show that entrainment and mixing lead to a roughly twofold increase in the volume transport of newly formed dense waters by the time they reach their equilibrium depth (25). Similarly, the transport of low-salinity intermediate water in the Okhotsk Sea intensifies by more than a factor of two as it travels southward along the Sakhalin coast (6, 18). Our observed DSW production rate is thus consistent with the overturn of $\sim 2 \text{ Sv}$ between surface and intermediate layers (1, 26) that sustains the NPIW.

Although the present study confirms basic hypotheses of DSW formation through brine rejection, it also highlights the limitations of our understanding of this process. In addition to external buoyancy forcing,

the internal dynamics of the shelf region has to be incorporated into dense water formation models. Additionally, relation of surface heat loss to the actual brine production for various ice formation scenarios needs better understanding. Close observation of downstream evolution and modification of DSW is also crucial for establishing a quantitative link of the brine rejection to the global thermohaline circulation.

References and Notes

1. L. D. Talley, *J. Phys. Oceanogr.* **33**, 530 (2003).
2. J. L. Reid, *Intermediate Waters of the Pacific Ocean* (Johns Hopkins Oceanography Studies, 1965).
3. L. Talley, *J. Phys. Oceanogr.* **23**, 517 (1993).
4. L. D. Talley, *Deep Sea Res.* **38**, S171 (1991).
5. K. Kitani, *Bull. Far Seas Fish. Res. Lab.* **9**, 45 (1973).
6. S. Gladyshev, S. Martin, S. Riser, A. Figurkin, *J. Geophys. Res.* **105**, 26281 (2000).
7. G. F. N. Cox, W. F. Weeks, *J. Glaciology* **13**, 109 (1974).
8. T. Markus, C. Kottmeier, E. Fahrbach, in *Antarctic Sea Ice: Physical Processes, Interactions and Variability*, M. O. Jeffries, Ed. (Washington, DC, American Geophysical Union, 1998).
9. S. R. Rintoul, in *Ocean, Ice, and Atmosphere: Interaction at Antarctic Continental Margin. Antarctic Research Series vol. 75*, S. S. Jacobs and R. Weiss, Eds. (American Geophysical Union, Washington, DC, 1998).
10. B. Rudels, R. Muench, J. Gunn, U. Schauer, H. Friedrich, *J. Marine Systems* **25**, 77 (2000).
11. J. Schumacher, K. Aagaard, C. Pease, R. Tripp, *J. Geophys. Res.* **88**, 2723 (1983).
12. T. J. Weingartner, D. J. Cavalieri, K. Aagaard, Y. Sasaki, *J. Geophys. Res.* **103**, 7647 (1998).
13. G. Manzella, R. Meloni, P. Picco, in *Oceanography of the Ross Sea, Antarctica*, G. Spezie and G. Manzella, Eds. (Springer-Verlag, Milan, Italy, 1999).
14. L. D. Talley et al., *Geophys. Res. Lett.* **30**, 1159, doi:10.1029/2002GL016451 (2003).
15. G. D. Williams, N. L. Bindoff, *Deep Sea Res.* **50**, 1373 (2003).
16. J. Hays, J. Morley, *Deep Sea Res.*, in press.
17. L. Keigwin, *Paleoceanography* **13**, 323 (1998).
18. S. Gladyshev, R. Talley, G. Kantakov, G. Khen, M. Wakatsuchi, *J. Geophys. Res.* **108**, 3186 (2003).
19. Measurements were conducted with an upward-looking RD Instruments Acoustic Doppler Current Profiler (ADCP) and a Seabird Seacat Conductivity-Temperature-Depth (CTD) sensor. Data were sampled at 15-min intervals.
20. S. Martin, R. Drucker, K. Yamashita, *J. Geophys. Res.* **103**, 27771 (1998).
21. D. Chapman, G. Gawarkiewicz, *J. Phys. Oceanogr.* **27**, 555 (1997).
22. K. I. Ohshima et al., *J. Phys. Oceanogr.*, in press.
23. R. R. Dickson, J. Brown, *J. Geophys. Res.* **99**, 12319 (1994).
24. E. Fahrbach, S. Harms, G. Rohardt, M. Schröder, R. Woodgate, *J. Geophys. Res.* **106**, 2761 (2001).
25. J. F. Price, M. Baringer, *Progr. Oceanogr.* **33**, 161 (1994).
26. A. M. Macdonald, *Progr. in Ocean.* **41**, 281 (1998).
27. J. Maslanik, J. Stroeve. Defense Meteorological Satellite Program (DMSP) SSM/I daily polar gridded brightness temperatures. Boulder, CO: National Snow and Ice Data Center, CD-ROM (1990).
28. D. Cavalieri, *J. Geophys. Res.* **99**, 12561 (1994).
29. K. I. Ohshima, T. Watanabe, S. Nishihashi, *J. Meteorol. Soc. Jpn.* **81**, 653 (2003).
30. This work was supported through the National Science Foundation OCE-9811958 and by Hokkaido University (ship support). Technical support was provided by the Oceanographic Data Facility and the Instrument Development Group at Scripps Institution of Oceanography, and by the captain and crew of the R/V Professor Khromov.

2 July 2003; accepted 30 October 2003